The real area of nanoporous catalytic surfaces of gold and palladium in aqueous solutions

U. P. Do[1]
F. Seland[2]
E. A. Johannessen[1]

Received: date / Accepted: date

[1]Department of Microsystems, Faculty of Technology, Maritime and Natural Sciences, University College of Southeast Norway, Raveien 215, 3184 Borre, Norway

[2]Department of Materials Science and Engineering, Faculty of Natural Sciences and Technology, Norwegian University of Science and Technology, NTNU 7491 Trondheim, Norway

Corresponding author, E. A. Johannessen: eaj@usn.no

Keywords: surface area, porous electrodes, catalytic properties, palladium, gold.

Abstract:

The determination of the real, or active, area of a catalytic surface is a key requirement to understand or quantify parameters related to its electrochemical behaviour. There are several experimental methods available, but none of them seems to be universally applied in literature. The choice of method is particularly important when evaluating electrodes made from materials that may interact with the analyte such as gold (Au) and palladium (Pd). A comparable analysis has therefore been made which includes four *in situ* methods (oxide formation, double layer capacitance, iodine adsorption and electrocatalysis of the Hexacyanoferrate (II/III) reductant-oxidant couple), and two *ex situ* methods (scanning electron microscopy and atomic force microscopy). It was found that measurements of oxide formation and the double layer capacitance gave the largest real surface area whereas scanning electron microscopy gave the smallest. Considering nanoporous Pd electrodes, the surface area ratio (the ratio between the real and geometric surface area) ranged from 0.8 (scanning electron microscopy) to 75.4 (oxide formation) and 76.5 (double layer capacitance). The corroboration between the results suggests that oxide formation and double layer capacitance provide the most accurate way of determining the real surface area for the electrode system investigated in this paper.

1 Introduction

The area of an electrode surface is normally defined by its physical dimensions and converted to a corresponding metric or imperial unit. This may be the true area for an ideally flat surface, but most real surfaces consist of micro- and nanotopographic structures and trenches that are not visible on the macroscopic scale. This surface topography may add a substantial increase to the effective surface area of the electrode, where the ratio between this real area (A_{real}) and the geometric surface area (A_{geo}) is defined as the *surface area ratio* (A_{real}/A_{geo} - which is sometimes also referred to as *roughness factor* in literature). A large surface area ratio would create a higher number of chemically reactive sites and may give the impression of a more active catalyst compared to a smoother surface of the same material. Consequently, a large surface area ratio would be an important property for electrodes with a small geometric area in order to improve their catalytic performance. This comes from the fact that most of the kinetic parameters that have been published (related to a specific electrochemical reaction catalysed by the electrode as well as the electrical double layer properties) is referred to the geometric surface area. Hence, the determination of the real surface area is a key requirement to separate the inherent catalytic properties of a material (the "turn-over frequency", or the amount of reactions at an active site for a given time interval) from that related to the surface area ratio.

The most common *in situ* methods used to determine the real surface area are based on electrochemistry, where the charge related to an adsorption process or the current generated from a reductant-oxidant (redox) reaction is measured as a function of the effective surface area available. Measurements on oxide formation and double layer capacitance are the most predominant as they are easy to perform, but also adsorption of specific probe molecules from the solution have been used [1-2]. The surface topography plays an important role here since the choice of molecular sizes used in the adsorption studies may render the probe molecules too large to access cracks, pores or grain boundaries that contribute towards the surface area [3]. Also, if the topography is smaller than the diffusion layer of the electroactive species used for the determination of the real surface area, any contributions from this topography will be masked away [4]. The type of probe molecules is also important for a given material system. For example iodine chemisorption, commonly used to determine the surface area of Au electrodes [5], may not be suitable for Pd electrodes because Pd atoms have an ability to re-order and change the surface structure in the presence of adsorbed iodine [6-7]. Similar to the effect of iodine chemisorption on Pd electrodes, underpotential deposition of metals (UPD) could result in phase transformations between the electrode metal and the UPD metals (e.g. Ag and Cu) causing surface reconstruction and a change in surface area [8-10]. Moreover, the UPD region is easily interfered with hydrogen and oxygen adsorption [4].

The most common *ex situ* methods used to determine the surface area are based on the adsorption of probe molecules from a gas phase, X-ray diffraction, porosimetry and microscopy [11-13]. The adsorption of probe molecules from the gas phase, also known as the Brunauer–Emmett–Teller (BET) method, is achieved by determining the change in mass of the sample before and after gas adsorption. Like all *ex situ* methods, it measures the total surface area and not the electrochemical active area [4]. It is easily interfered with hydrogen and oxygen adsorption [1]. X-ray diffraction gives information on crystallite size and the degree of dispersion of the material [14-15], but should be used with other appropriate techniques for surface area measurements in order to achieve a complete analysis of the surface morphology [4]. Porosimetry is used to find the distribution of pores in a material and estimates the specific area of the non-porous solid part [16]. This method employs pressurised mercury, which could disrupt the pore system of thinned walled materials and is also a difficult technique to implement [11].

Microscopy offers resolution from the macroscopic (mm) to the sub nm scale, depending on the type of microscope used (optical, ellipsometry, spectroscopy, scanning/transmission electron microscopy (SEM/TEM) or scanning tunnelling microscopy (STM) [4]. Atomic force microscopy (AFM) permits direct measurements of the topographic features, but the spatial resolution of these is limited to the size of the microscope probe [17]. In general, microscopy offers examination of only a small part of the total electrode surface at the magnifications required to resolve microtopographic features. This part only gets smaller with higher magnifications, and one needs to assume that the rest of the electrode surface bears similar structural traits if the real surface area is determined using microscopic techniques. Although AFM has the option to calculate the surface area directly through the imaging software, manual investigation using traditional optical or electron microscopes is a time consuming process where the area of topographic structures needs to be individually assessed. This can be performed according to the ISO 25178 standard, but this is quite extensive and is meant to be a framework to standardise computer algorithms used for 3D surface texture analysis.

Although the real surface area is determined experimentally, there are no universal methods available that can be applied to any electrode material. This is particularly important for electrodes made from gold (Au) and palladium (Pd) which are commonly used instead of platinum (Pt). Both Au and Pd offer desirable properties as electrode materials since they are relatively easy to implement in microfabrication (lower melting temperatures than Pt), they offer good electrical conductivity, reasonable chemical stability, tunable pore size and a relatively open pore network [18-19]. Pd is commonly used as a catalyst of automotive exhausts (especially NO reduction) [20], formic acid oxidation [21-22], oxygen (O_2) reduction in low temperature fuel cells [23], and water purification [24]. Pd is also able to absorb hydrogen by more than 800 times its own volume [7, 25]. In contrast, Au is commonly found in electrochemical sensors (immuno-, DNA-, enzyme-based- small molecule- and Raman sensors [18]) due to its biocompatible nature and the ease of attachment of probe molecules.

The most common method used to determine the real surface area of Pt electrodes is the standard hydrogen underpotential deposition (H_{UPD}) [4, 26], which has been extended by McCrum and Janik to identify the proportion of 111, 100 and 110 sites based on calculated coverages of adsorbed hydrogen and hydroxide [27-28]. As this method works very well for Pt electrocatalysts, it fails to do the same for Au and Pd electrodes. The desired monolayer formation of adsorbed hydrogen required to estimate the active area does not form on the surface of the Au [5], whereas Pd would absorb hydrogen beyond the monolayer concentration [25].

Consequently, this study focuses on some selected alternative methods that are available in our laboratories to estimate the real surface area of Pd and Au electrodes. The *ex situ* methods include SEM and AFM microscopy while the *in situ* methods include oxide formation and reduction from cyclic voltammetry [29], double layer capacitance from electrochemical impedance spectroscopy, adsorption and stripping of iodine (I) and finally the electrochemical response of the hexacyanoferrate (II/III), $[Fe(CN)_6]^{4-/3-}$ redox couple, with subsequent use of the Randles-Sevcik equation. A comparative analysis was then performed to investigate the usability, accuracy and potential source of errors of these methods.

2 Materials and Methods

2.1 Electrode fabrication

Nanoporous alumina (AAO) membranes with a diameter of 13 mm, a thickness of 60 µm and pore diameters of 100 and 200 nm were used as electrode substrates (Anodisc 6809-7013 and 6809-7023, Fisher Scientific, UK). Pellets of Pd and Au (code: EVMPD35SHOT and EVMAUXX40G, supplied by Kurt J. Lesker, US) were used to deposit thin metal films with a thickness of 100 and 200 nm respectively by e-beam evaporation. The different pore diameters were chosen to investigate the relationship between the surface topography and metal deposition thickness. The substrates were assembled in a custom-made holder taking 10 membranes in one batch. The substrates were rotated at an angle during the evaporation process in order to improve the material coverage inside the vertical walls of the pores. The samples were diced into pieces of 0.1 cm^2 and attached to a standard 1 x 3 $inch^2$ glass slide by silicone adhesive (3140 RTV Coating, Dow Corning, US). Copper wires were bonded to the sample using silver epoxy (EPO-TEK® EE129-4, Epoxy Technology, Inc., US) to form an electrical connection to the electrodes. Additional silicone adhesive was then applied to electrically insulate the copper wires from the aqueous test solution.

2.2 The *ex situ* surface characterisation methods

Surface analysis was done both prior to and after metal deposition by a SEM microscope (LEO 1550, ZEISS, Germany). The analysis of the SEM images was performed using an image analysis software (ImageJ, National Institutes of Health, US), which converted the SEM image into pixels of black and white. The pores will be visible as white pixels, whereas the remaining surface consists of black pixels. Based on the scale bar in every picture, the image analysis software calculates the effective (black) surface area, and with the surface area ratio obtained by dividing the calculated surface area by the geometrical area of the SEM image. A direct scan of the surface topography was performed both before and after metal deposition by an AFM (XE-200, Park Systems Co., USA) operating in a non-contact mode. The cantilevers had a tip height of 10-15 µm, guaranteed tip radius < 10 nm (typical < 7 nm), resonance frequency of 330 kHz and a force constant of 42 N/m (PPP-NCHR 3U, Nanosensors TM, Switzerland). The material composition was analysed before and after metal deposition by an Energy Dispersive X-Ray Spectroscopy, EDS, (SU3500, Hitachi, Japan).

2.3 The *in situ* surface characterisation methods

2.3.1 Oxide formation (OF)

Hydrogen adsorption-desorption studies used for Pt electrodes was not found to be suitable for metals such as Au or Pd [4]. A viable alternative would be to quantify the charge affiliated with the oxide formation and the subsequent reduction as recorded from a cyclic voltammogram (CV) when the electrode is immersed in 0.5 M H_2SO_4 [7]. A Pt coil (P/3640/89, Fisher Scientific Limited, UK) was used as the counter electrode. All potentials recorded in this study are referred to a standard Ag|AgCl reference electrode in 4 M saturated KCl (Thermo Scientific, USA). The

cyclic voltammograms (CVs) of the electrodes were obtained at a scan rate of 50 mV s^{-1} over a potential range from 0 - 1.25 V for the Pd coated electrodes, and 0 - 1.5 V for the Au coated electrodes using a potentiostat (Versastat 3, Princeton Instruments, USA). The reduction charge of the palladium oxide was calculated as the integrated current with time corresponding to the potential region of 0.2 - 1.2 V in the negative-going scan (considering that the oxide being formed is only PdO, and that its reduction is complete at around 0.2 V [7]). The charge density associated with the reduction of one monolayer of PdO, 424 µC cm^{-2} [7], was then used to find the real surface area of the Pd electrodes. Analogously, the anodic charge from the gold oxidation was calculated from a CV in the potential range from 1 V, and up to the Burshtein minimum value (of about 1.4 V), where a monolayer of gold oxide is formed. The cathodic charge from the Au-oxide reduction was calculated in the potential region of 0.7 - 1.1 V. The charge density associated with a monolayer of gold oxide, 386 µC cm^{-2} [2, 30], was then used to find the real surface area of the Au electrodes.

2.3.2 Double layer capacitance measurement (DLC)

Measurements of the double layer capacitance at the electrode-electrolyte interface were performed in a deaerated solution of 0.5 M H_2SO_4 using an electrochemical impedance spectroscope (EIS) over a frequency range from 10 mHz to 10 kHz (IM6, Zahner-elektrik GmbH, Germany). A constant potential of 0.3 V was applied for both the Pd and Au electrodes together with a 5 mV amplitude sinusoidal AC potential perturbation. The electrical equivalent circuit, shown in Figure 1, was used in this work to estimate the double layer capacitance and ohmic resistance. The circuit includes the uncompensated ohmic resistance (R_o) between the working and reference electrodes in series with the double layer interface, comprising of a charge transfer resistance (R_c) parallel with the double layer capacitance, the latter represented by a constant phase element (CPE) as validated by the F-ratio test for adding a parameter. The simulation function (SIM) of the Zahner potentiostat was then used to find the charge transfer resistance, the Ohmic resistance and the CPE parameters including the constant representative (Q) and the exponent (n) from a fitting of experimental impedance data to the circuit in Figure 1. The transfer function of the model is fitted to the experimental data by a Complex Non-linear Regression Least-Squares (CNRLS) routine which changes the parameters of the model until the weighted total deviation between the model's transfer function and all experimental data points is minimized [31]. The double layer capacitance was then extracted from the CPE parameters by the following equation [32-33]:

$$C_{dl} = [Q(R_0R_C/(R_0+R_C))^{1-n}]^{1/n} \quad (1)$$

Since the double layer capacitance of an ideally smooth surface at 0.3 V is estimated to be 24.5 µC cm^{-2} [34] for the Pd electrodes and 60 µC cm^{-2} [30] for the Au electrodes, the real surface area of the Pd and Au electrodes was found by dividing the double layer capacitance value with this area specific double layer capacitance.

2.3.3 Iodine adsorption (IA)

The iodine adsorption studies were performed by first immersing the electrodes in a fresh deaerated solution of 1 M H_2SO_4 for 5 minutes. The solution had been deaerated for 15 min with N_2 before the experiment started and also throughout the experiment. The CVs of both the Pd and Au electrodes were then obtained in the potential region of 0 to 1.2 V for the Pd electrodes

and 0 to 1.5 V for the Au electrodes, at a scan rate of 10 mV s^{-1}. The electrodes were then immersed into a deaerated solution of 1 mM KI in 1 M H_2SO_4 mixture for 5 minutes and then rinsed thoroughly three times in separated fresh deaerated solutions of 1 M H_2SO_4. The CV's were then repeated for the same settings with the electrodes immersed in a fresh deaerated 1 M H_2SO_4 *s*olution. The anodic oxidation of chemisorbed iodine follows the reaction [5]:

$$I_{ad} + 3H_2O \rightarrow IO_3^- + 6H^+ + 5e^- \quad (2)$$

The active surface area of the Pd electrode can then be determined by the following relation [5]:

$$A = Q_{iod}/nF\Gamma_I \quad (3)$$

where A is the area (cm^2), Q_{iod} is the electrolytic charge (C) from the oxidation of the adsorbed iodine at the electrode; n is the number of electrons involved in the oxidation process (n = 5 in this case); F is Faradays constant (96485 C mol^{-1}); and Γ_I ($1.04x10^{-9}$ mol cm^{-2}) is the calculated iodine packing density [5]. The net oxidation charge of iodine Q_{iod} in Eq. (3) was found from subtracting the background charge (Q_{bg}) obtained in the iodine free electrolyte from the total charge (Q_{tot}) obtained in the iodine containing electrolyte:

$$Q_{iod} = Q_{tot} - Q_{bg} \quad (4)$$

The potential limits of the integration for the charge calculation and the background charge Q_{bg} are defined in section 3.4.

2.3.4 Hexacyanoferrate (II/III) electrocatalysis (FE)

The hexacyanoferrate redox couple is often used as a model electrochemical reaction with its simple and fast one-electron charge transfer on many surfaces.

$$[Fe(CN)_6]^{3-} + e^- \leftrightarrow [Fe(CN)_6]^{4-} \quad (5)$$

This reaction leads to a well-defined redox wave on both sides of the reversible potential (depending on initial concentrations) during potential cycling. Finding the peak current density for a range of sweep rates allows us to estimate the area of the electrode employing the Randles–Sevcik equation. This equation describes a linear relation between the diffusion controlled peak current and the square root of the sweep rate [35-37]:

$$I_p = (0.4463)nFAC_0(nFvD/RT)^{1/2} \quad (6)$$

where I_p is the peak current (reduction or oxidation), *n* is the number of electrons participating in the redox reaction, *F* is Faradays constant (C mol^{-1}), *A* is the area of the electrode (cm^2), C_0 is the concentration of the reacting species in the bulk solution (mol cm^{-3}), *v* is the scan rate of the applied potential (V s^{-1}), *D* is the diffusion coefficient of the reacting species (reduced or oxidized) in the solution (cm^2 s^{-1}), *R* is the gas constant (J K^{-1} mol^{-1}) and *T* is the absolute temperature (K). Considering a solution at 25°C, the Randles–Sevcik equation becomes:

$$I_p = (2.69x10^5)n^{3/2}AD^{1/2}C_0v^{1/2} = \text{Slope x } v^{1/2} \quad (7)$$

In this case, n = 1, and the diffusion coefficients in a similar electrolyte are reported to be

$D_{Fe(CN)63-}$ = 7.26x10^{-6} cm^2 s^{-1} and $D_{Fe(CN)64-}$ = 6.67x10^{-6} cm^2 s^{-1} by Konopka and McDuffie [38]. The electrodes were immersed in a solution of 3 M KCl and 10 mM of $K_3Fe(CN)_6$. The CVs were obtained over a potential range of 0 to 0.6 V with a scan rate ranging from 10 to 400 mV s^{-1}. Although the reduction product $[Fe(CN)_6]^{4-}$ will be formed on the electrode surface during the cathodic sweep and be oxidised back to $[Fe(CN)_6]^{3-}$ in the anodic sweep within the given scan rates, only the bulk concentration of $[Fe(CN)_6]^{3-}$ is known. Hence the real surface area, *A,* was estimated from the slope of the linear relation between the cathodic peak current, I_p and $v^{1/2}$.

3 Results and discussion

3.1 Microstructural evaluation

The metal is deposited on the interpore region in a similar way to that observed from sputtered Pt atoms on porous AAO substrates [39], and are shown in Figure 2a,b and Figure 2c,d for the Pd and Au electrodes, respectively. Similar images of the native AAO substrates are reported in a previous study from our group (Figure 2a,b in [27]). The interpore region, taken as the real area of the substrate, was estimated from the two dimensional (2D) SEM images using the ImageJ software and corresponds to the scanned area with all pores subtracted. Not surprisingly, such a 2D consideration generates a surface area ratio (real area vs geometric area ratio) that is significantly lower than 1, due to the large number of pores in the electrode substrate. A better *ex situ* approach is therefore to estimate the three dimensional (3D) surface topography with an AFM both prior to and after the deposition of metal (Figure 3). Although SEM has the capability to offer some information about surface topography and structure, this information is much easier quantified with an AFM. It is clear however, that the surfaces appear to be covered by “rounded” objects or particles, especially around the rims of the pores. Such features are a typical signature of “cliff” and “shadow” tip-induced artefacts, also known as tip-sample convolution effects. These effects are critically related to the actual inclination of the working cantilever, the tip geometry and the obstructive contacts between the working tip’s planes / edges and the adjacent particle groups on the scanned surface [40-41]. Hence, tip convolution effects may mask the real surface geometry and thus generate errors in the measurement of the surface area. The results obtained from both the SEM and AFM images are summarized in Figure 4 showing that the surface area ratio obtained by the AFM is around 40 to 50 times larger.

In general, the surface area ratio of the metal coated AAO substrates was found to be larger than the uncoated ones. The deposited metal results in a thickening of the rims or walls of the interpore region, which increases the surface roughness and consequently the real surface area (as suggested from the SEM and AFM images). The larger surface area from Pd can be explained from an initial cluster formation of the Pd atoms which grow in size and merge into a uniform (porous) layer. The Au atoms stack more densely on the surface and grow into a uniform layer without any observable clusters. It was also observed that the electrodes with 100 nm pores have a larger surface area ratio (irrespective of the metal coating) than those with 200 nm pores due to an inherent lower porosity of the substrate.

3.2 Oxide formation (OF)

Cyclic voltammograms displaying the oxide formation and reduction for both the Au and Pd electrodes are presented in Figure 5. In the positive-going scan, the growth of oxide commences at about 0.7 V for the Pd electrode and about 1.1 V for the Au electrode and leads to a plateau-like region until the reverse potential is reached (marked as 1 in Figure 5). Extensive research has been done in literature, both experimentally and theoretically, in order to understand the oxide formation and growth on noble metal electrodes [7, 42-43]. The early stage of oxide formation has not been fully resolved despite massive attention over the last decades (e.g. Farkas et al.). In this work we consider only the formation of thin anodic oxide films (α-oxides) through a simplified reaction mechanism directly from water to Pd oxide or Au oxide involving the transfer of two electrons. The reduction of the thin oxide layers is clearly seen in the voltammograms in the area 0.5 to 0.3 and 1.0 to 0.8 V in the negative-going sweep for Pd oxide and Au oxide reduction, respectively (marked as 2 in Figure 5). Thicker oxides (β-oxides) are only formed when sweeping to higher anodic potentials [7, 44].

In this work, the charge associated with the oxide formation on the Pd electrodes (peak 1 in Figure 5a) was measured to 3.24 ± 0.13 mC and 2.84 ± 0.10 mC for the electrodes equipped with 100 and 200 nm pores, respectively. The corresponding real surface area was calculated to 7.64 ± 0.31 cm^2 and 6.69 ± 0.24 cm^2, which translates to a surface area ratio of 76.4 ± 3.1 and 66.9 ± 2.4 respectively. The charge associated with the oxide reduction of 3.20 ± 0.10 mC and 2.81 ± 0.30 mC for the Pd electrodes equipped with 100 and 200 nm pores (peak 2 in Figure 5a), gave a corresponding real surface area of 7.54 ± 0.23 cm^2 and 6.63 ± 0.70 cm^2. The surface area ratio was in this case 75.4 ± 2.3 and 66.3 ± 7.0 respectively.

There is a small but distinct difference in the surface area ratio based on the calculated value from the oxide formation peak or the oxide reduction peak with the former being larger than the latter. In acidic solutions, Pd is known to have a much higher dissolution rate than in alkaline solutions. Thus any dissolution of Pd (eg. $Pd \rightarrow Pd^{2+} + 2e^-$) will contribute to the overall anodic charge during oxide formation, whereas Pd^{2+} will diffuse away from the surface and not contribute to the total charge observed during oxide reduction [45]. Hence the reduction charge would be more accurate, and should be the number considered when calculating the real surface area in this case.

Considering the Au electrodes, the anodic peak associated with oxide formation (peak 1 in Figure 5b), starts at 1.1 V and stops at the Burshtein minimum (about 1.45V). The maximum value was observed at 1.23 V for the electrodes equipped with 100 nm pores, and 1.26 V for the electrodes equipped with 200 nm pores. The reduction process appears as a single reduction step (peak 2 in Figure 5b) with a maximum at 0.92 V for both the Au electrode samples. The charge associated with oxide formation for the Au electrodes with 100 nm pores was measured to 1.64 ± 0.15 mC, which corresponds to a surface area of 4.25 ± 0.36 cm^2. The charge associated with oxide reduction was measured to 1.62 ± 0.13 mC with a corresponding surface area of 4.20 ± 0.33 cm^2. Hence, the surface area ratio was calculated to 42.5 ± 3.6 (oxidation) and 42.0 ± 3.3 (reduction). Considering the Au electrodes with 200 nm pores, the charge associated with the oxide formation was 1.36 ± 0.10 mC which corresponds to a surface area of 3.52 ± 0.15 cm^2. The charge associated with the oxide reduction was measured to 1.34 ± 0.05 mC which corresponds to a surface area of 3.47 ± 0.13 cm^2. The resulting surface area ratio was calculated to 35.2 ± 1.5 (oxidation) and 34.7 ± 1.3 (reduction).

As observed for the Pd electrodes, there is a small discrepancy between the charges associated with the oxidation and reduction step also for the Au electrodes resulting in a larger surface area ratio with the calculation based on the oxidation charge. Due to the acidic environment, some of the Au could dissolve ($Au \rightarrow Au^{+} + e^{-}$) and contribute to the overall anodic charge during oxide formation. With the gold ion diffusing away, it will not be contributing to the total charge during the oxide reduction step. Hence, the real surface area should be calculated from the reduction step.

3.3 Double layer capacitance measurement (DLC)

The EIS results from the measurements conducted in 0.5 M H_2SO_4 at 0.30 V are given in Figure 6, and the simple equivalent circuit (Figure 1) fits well to the data recorded for the Pd electrodes. Based on the curve fitting, the double layer capacitance was calculated to 184.9 $\pm$ 7.7 μF and 157.1 $\pm$ 8.3 μF for the Pd electrodes equipped with 100 and 200 nm pores, respectively. This corresponds to a real surface area of 7.65 $\pm$ 0.31 cm^2 and 6.41 $\pm$ 0.34 cm^2, resulting in a surface area ratio of 76.5 $\pm$ 3.1 and 64.1 $\pm$ 3.4. For the Au electrodes, the charge-transfer resistance R_c (Figure 6b) is much larger than the ohmic resistance R_o (about 23 x 10^6 times) and could therefore be neglected. The equivalent circuit in Figure 1 could be changed into the Ohmic resistance R_o in series with the CPE (see inset (ii) in Figure 6b) which is in agreement with the circuit used to estimate the double-layer capacitance of the Au electrodes [30]. However, we still used the equivalent circuit in Figure 1 to fit the data recorded from the Au electrodes so that the double layer capacitance of the Au electrodes could be compared to those of the Pd electrodes. Based on the curve fitting, the double layer capacitance values were calculated to 250.4 $\pm$ 10.3 μF and 200.9 $\pm$ 35.5 μF for the Au electrodes equipped with 100 and 200 nm pores respectively. This corresponds to a real surface area of 4.17 $\pm$ 0.17 cm^2 and 3.35 $\pm$ 0.59 cm^2. The resulting surface area ratio was calculated to 41.7 $\pm$ 1.7 and 33.5 $\pm$ 5.9 for the Au electrodes equipped with 100 and 200 nm pores.

3.4 Iodine adsorption (IA)

The results from the CV plots of the iodine pretreated Pd and Au electrodes immersed in 1 M H_2SO_4 are shown in Figure 7. It was found that the disordered top-most Pd layers are stripped during the anodic process (the forward scan – peak 1, Figure 7.a), just before the adsorbed iodine I_{ads}^- are desorbed, resulting in a smoothening of the Pd surface [6]. This smoother and more “planar” surface reduced the charges obtained from the main oxide reduction peaks (the reverse scan – peak 2, Figure 7.a). By considering peak 2 within the potential region of 0.2 – 0.7 V, the charges accumulated from an untreated Pd electrode with 100 nm pores were measured to 3.1 $\pm$ 0.1 mC which is 12 % higher than the charges associated with the same electrode pretreated with iodine (2.8 $\pm$ 0.3 mC). The corresponding values for Pd electrodes with 200 nm pores were 2.6 $\pm$ 0.1 mC and 1.9 $\pm$ 0.1 mC respectively (or 38% higher). Therefore, the untreated samples are shown in comparison and act as a background reference from which the iodine adsorption measurements are subtracted. The total charges of the electrodes pretreated with iodine (Q_{tot}) and the background charges of the untreated electrodes (Q_{bg}) were calculated in the potential region of 0.7 – 1.2 V. If we subtract Q_{tot} (6.9 $\pm$ 0.1 mC and 5.1 $\pm$ 0.3 mC for the Pd electrodes equipped with 100 and 200 nm pores) with Q_{bg} of the untreated electrodes (3.4 $\pm$ 0.1 mC and 2.8 $\pm$ 0.1 mC respectively), the charges obtained from iodine oxidation (Q_{iod}) were 3.6 $\pm$ 0.3 mC for Pd electrodes equipped with 100 nm pores and 2.3 $\pm$ 0.4 mC for Pd electrodes

equipped with 200 nm pores. The surface area, based on Eq. (4) and Eq. (5), was calculated to 7.18 ± 0.63 cm^2 and 5.76 ± 0.72 cm^2, resulting in a surface area ratio of 71.8 ± 6.3 and 57.6 ± 7.2 for the Pd electrodes equipped with 100 and 200 nm pores. If one were to calculate the surface area based on the oxide reduction peaks alone, the following values would be obtained: untreated and iodine treated Pd electrodes with 100 nm pores (7.42 ± 0.34 cm^2 and 6.6 ± 0.6 cm^2 respectively), untreated and iodine treated Pd electrodes with 200 nm pores (6.24 ± 0.23 cm^2 and 4.5 ± 0.3 cm^2 respectively). Hence the surface area ratio of the untreated electrodes obtained from the oxide reduction process (74.2 ± 3.4 and 62.4 ± 2.3 for 100 and 200 nm pore electrodes) corresponds more closely to that obtained from the iodine oxidation peaks prior to stripping of the Pd top layers (also comparable to the results from section 3.2).

Considering the Au electrodes, the total charge (Q_{tot}), calculated over a potential range from 1 to 1.45 V (peak 1 in Figure 7.b), would also include the charges associated with the oxidation of adsorbed iodine and the oxidation of Au. The total charge associated with the oxidation of Au will in this case form a background charge Q_{bg}. The magnitude of Q_{bg} from untreated electrodes is equal to the charge from the oxide reduction process and also equal to the oxide reduction charge of the iodine-treated Au electrodes (1.7 ± 0.1 mC and 1.4 ± 0.1 mC for the 100 and 200 nm pores electrodes, respectively). Hence, Q_{bg} can be found from the charge associated with the oxide reduction process of the iodine-treated Au electrodes - peak 2 in Figure 7.b. After subtracting Q_{bg} from Q_{tot} (Eq. (5)), the charges obtained from the iodine oxidation process (Q_{iod}) was calculated to 2.1 ± 0.4 mC and 1.6 ± 0.2 mC for the Au electrodes equipped with 100 and 200 nm pores, respectively. Based on Eq. (4), the corresponding area was found to be 4.18 ± 0.83 cm^2 and 3.29 ± 0.33 cm^2 for the Au electrodes equipped with 100 and 200 nm pores, resulting in a surface area ratio of 41.8 ± 8.3 and 32.9 ± 3.3, respectively.

3.5 Hexacyanoferrate (II/III) electrocatalysis (FE)

The cathodic peak currents obtained from the hexacyanoferrate electrocatalysis experiments using Pd and Au electrodes are given as a function of the square root of the scan rate in Figure 8 using the Randle-Sevcik equation. The top left hand column (LHC) insets include the representative CVs obtained from the experiments on electrodes equipped with (i) 100 nm and (ii) 200 nm pores. The bottom right hand column (RHC) insets of
show the estimated surface area based on the linear slopes derived from the recorded peak currents. The CVs obtained from the redox couple $[Fe(CN)_6]^{3-/4-}$ gives well-defined oxidation and reduction peaks (labelled P.1 and P.2 respectively) during the forward (anodic) and reverse (cathodic) scan. (Figure 8, insert (iii)).

The cathodic currents from the reduction step was found to be larger than the anodic currents from the oxidation step in all of the experiments. This can be explained by the constant bulk concentration of the initial reactant $[Fe(CN)_6]^{3-}$ being larger than that of the reaction product $[Fe(CN)_6]^{4-}$ since some of the latter will diffuse away from the electrode surface before being reoxidised back to $[Fe(CN)_6]^{3-}$. The diffusion coefficient of the $[Fe(CN)_6]^{4-}$ involved in the oxidation step is also lower than the diffusion coefficient of the $[Fe(CN)_6]^{3-}$ involved in the reduction step [38]. The results suggests that this is a diffusion limited process where the faster moving substrate species would yield a larger peak current.

The real electrode surface area derived from the cathodic peaks was found to be 5.14 ± 0.27 cm^2 and 4.17 ± 0.32 cm^2 for Pd electrodes equipped with 100 and 200 nm pores, respectively which corresponds to a surface area ratio of 51.4 ± 2.7 and 41.7 ± 3.2. Similarly, considering the

Au coated electrodes, the surface area was calculated to 3.49 ± 0.19 cm^2 and 2.78 ± 0.27 cm^2 for electrodes equipped with 100 and 200 nm pores, respectively, corresponding to a surface area ratio of 34.9 ± 1.9 and 27.8 ± 2.7.

3.6 Comparative analysis

The surface area ratios obtained from the different experimental methods are presented in table 1 and graphically illustrated in Figure 9
. The result yields a large range of values when comparing the different methods with each other, but some general trends are observed. The electrodes equipped with 100 nm pores have a larger surface area than the ones equipped with 200 nm pores. This mirrors the native AAO surface where the lower density of pores of the 100 nm membrane results in a larger effective surface area for any given geometry.

It was also found that the Pd coated electrodes exhibit a larger surface area than the Au coated electrodes. This can be explained by the cluster formation of the Pd layer resulting in a more uneven topography which again contributes toward the total surface area ratio.

Evaluating the *ex situ* methods first, the surface area of the electrodes was initially estimated from the 2D SEM images. A transition to a more complex 3D interpretation of the surface area was not performed, and hence this simplification meant that any area contributions in the vertical (z) direction were not considered. Consequently, the surface area ratio obtained from 2D SEM images would yield the lowest value and this method is only effective to determine the level of porosity (holes vs solid surface) of a specific electrode. In fact, the surface area ratio becomes synonymous with porosity using a 2D SEM approach. In contrast, the missing information in the z-direction is recorded using AFM, which provides a full assessment of the surface topography of a sample. However, one of the most important problems with AFM characterization is the appearance of artefacts caused by the tip-sample convolution effect. Artefacts will generate fraudulent features that modify the real surface topography and compromise the reliability of any dimensional information [46]. It is in particular the quality of the AFM images of high aspect ratio features, such as sharp spikes, deep holes, trenches, rods and cylinders that depends on the inclination of the working cantilever as well as the sharpness and geometry of the tips [40]. A typical example is the broadened images of sharp spikes recorded with blunt tips [47], shallow images of deep holes, pits and trenches [46], and the appearance of “cliff-like” structure or “shadow” occurrence of rod and cylinder like features with steep sidewalls [48-50]. Considering these challenges, the obtained surface area ratio will most likely be lower than its true value. The area of the pores would also need to be considered, but this fraction of the geometrical surface area (0.2 – 0.4) obtained by the SEM was small compared to the surface area ratio (24 -38) obtained with the AFM (Table 1).

Considering the *in situ* methods, four different electrochemical techniques were selected and compared with each other. In contrast to imaging (SEM) or mechanical surface scanning (AFM), electrochemical methods require substrates with an electrical conducting layer on top. The utilization of molecular scale probe molecules (such as the adsorption of Iodine, Hexacyanoferrate (II/III), oxygen), or the charge accumulation on the surface, offers the potential to penetrate any available crack, hole or crevice at the molecular scale. It was found that the lowest surface area ratio was obtained from the work on the hexacyanoferrate $[Fe(CN)_6]^{3-/4-}$ redox couple. The porous nature of the surface may be considered as a kind of nanoelectrode ensemble where the catalytic active surfaces separated by the pores may exhibit

micro/nanoelectrode behaviour [51]. The diffusion mediated transport may be either (i) radial, (ii) one dimensional linear, or (iii) a combination of these two depending on the scan rate and separation distances between these catalytic active areas. The linear relationship between the peak currents and the square root of the scan rate found in this study suggests that mass transfer to the electrode surface is controlled by a one dimensional linear diffusion. If this diffusion layer is larger than the surface topography, these topographic structures will be masked away within the diffusion layer. Any area contribution from these will not be considered and the surface area will appear smaller than what it really is. At the same time one should note that the size of the electrode samples used in this study was smaller than that recommended for the investigation of methods based on one dimensional diffusion limited transport [52]. The contribution of radial diffusion (edge effect) would promote diffusional transport of the redox couple at the electrode edges resulting in a larger current and apparent surface area than that obtained from a simple one dimensional (1D) model. Still, the real surface area found with the Hexacyanoferrate (II/III) redox couple suggests that masking of the surface topography would be the dominating parameter of these two.

The study on iodine adsorption was not governed by any diffusional limitation, which means that any available area of the electrode should be available for bonding to iodine. Further, the atomic scale of the iodine ion should also ensure that nm scale topographies should be included in this assessment. Hence, the surface area ratio of the Au electrodes estimated from this method is similar to the one obtained by the oxide formation and the double layer capacitance measurements. The surface area ratio of the Pd electrodes has the same behaviour as the surface area ratio of the Au electrodes. One special property of the Pd electrodes is that the anodic stripping of the disordered top-most Pd layers during the forward scan of CVs happens just before I_{ads} desorption occurs. This results in a smoothening of the Pd surface. Consequently, multiple CVs running on the Pd electrodes could strip all of Pd atoms on the electrode surface and eventually destroy the sample. Therefore, area determination of Pd electrodes based on iodine adsorption should be treated with caution.

The surface area ratio calculated from the oxide formation studies gives the largest values in this study. Although this method is applicable to both Pd and Au, it is considered to be less reliable than that based on hydrogen adsorption because the reliability decreases as the affinity of the metals towards oxygen increases [4]. Moreover when using the approach of determining the charge formation and reduction of oxide, the values for the reduction or the formation of one oxide monolayer are very important. The published values of charge densities from one oxide monolayer range from 386 $\mu C\ cm^2$ [2, 30], 390 $\mu C\ cm^2$ [4], 400 $\mu C\ cm^2$ [30] and 550 $\mu C\ cm^2$ [5] for AuO, and from 420 $\mu C\ cm^2$ [19] to 424 $\mu C\ cm^2$ [2, 7] for PdO [43]. Since these values were calculated theoretically or under different experimental conditions, one needs to be careful when choosing the correct value. The charge densities of 424 $\mu C\ cm^2$ (PdO) and 386 $\mu C\ cm^{-2}$ (AuO) used in this study were based on the fact of similar experimental conditions taken from literature [2, 7, 30]. In order to estimate the real surface area through charge measurements, one must know the potential at which one monolayer is known to form. In this work, we used the potential range of 0.2 – 1.25 V and 0.7 – 1.1 V in the negative-going scan for the Pd and the Au coated electrodes respectively [2, 7, 30]. For the Pd coated electrodes, the maximum potential of 1.25 V vs Ag|AgCl (or 1.45 V vs SHE) was used in this work as recommended by literature [29, 53]. For the Au coated electrodes, the determination of the potential where the Burshtein minimum current occurs is ambiguous which affects the choice of the potential range for the charge determination [54].

It was found that the surface area ratio calculated from the measurement of the double layer capacitance is similar to that calculated from the oxide formation method. One needs to pay

attention to the fact that the magnitude of the double-layer capacitance depends on the applied electrode potential and the electrolytes used [19]. It is therefore important to be aware of the potential range to which the double-layer capacitance is referred to [19], ranging from 17 to 25 $\mu F\ cm^2$ [34] for Pd and from 58 to 73 $\mu F\ cm^2$ for Au [30]. Still, the cross correlation of comparable data obtained from the measurements on the oxide formation and the double layer capacitance (two different methods) suggests that these values would offer the most correct representation of the real surface area for the Pd and Au electrodes.

4 Conclusions

The determination of the real surface area of the porous Pd and Au electrodes was investigated using commonly known surface characterisation methods. These included both *ex situ* and *in situ* type of analysis that have all been exploited in literature but their limitations for a given surface have not always been clearly addressed. Both SEM and AFM analysis is universally applicable for most solid surfaces (both conducting and non conducting) and gives structural information about surface architecture and geometry. These methods may not provide an accurate value of the real surface area due to limitations in the instrumentation (resolution) or the methodology used. Electrochemical methods are applicable for most conducting surfaces. Both iodine adsorption and electrocatalysis of the Hexacyanoferrate (II/III) redox couple gave larger surface area ratios than the *ex situ* methods. The largest values were obtained from the oxide formation and the double layer capacitance measurement since these methods did not cause any remodelling of the Pd surface nor were they subjected to any diffusion limited transport of reactants. The similar results in surface area obtained from both the oxide formation and double layer capacitance measurements act as a cross correlation increasing the confidence that the correct values were obtained. It is therefore important to choose a method to determine the surface area that is compatible with the system being investigated and the experimental conditions used.

Acknowledgements

The authors would like to thank the technical staff and colleagues at University College of Southeast Norway for their assistance in this work. The work was supported by the Ministry of Church and Education and The Research Council of Norway (Norfab project no. 245963/F50).

References

[1] M. Łukaszewski*, et al.*, "Electrochemical Methods of Real Surface Area Determination of Noble Metal Electrodes – an Overview," *International Journal of ELECTROCHEMICAL SCIENCE,* vol. 11, pp. 4442-4469, 2016.

[2] D. A. J. Rand and R. Woods, "The nature of adsorbed oxygen on rhodium, palladium and gold electrodes," *Journal of Electroanalytical Chemistry and Interfacial Electrochemistry,* vol. 31, pp. 29-38, 1971/06/01 1971.

[3] A. Kellomaki, "On the use of ethylene glycol and glycerol for surface area measurement," *Journal of Colloid and Interface Science,* vol. 105, pp. 270-272, 1985.

[4] S. Trasatti and O. A. Petrii, "Real surface area measurements in electrochemistry," *Journal of Electroanalytical Chemistry,* vol. 327, pp. 353-376, 1992/06/10 1992.

[5] J. F. Rodriguez*, et al.*, "Determination of the surface area of gold electrodes by iodine chemisorption," *Journal of Electroanalytical Chemistry and Interfacial Electrochemistry,* vol. 233, pp. 283-289, 1987/09/10 1987.

[6] J. B. Abreu*, et al.*, "Electrochemical digital etching in non-corrosive electrolyte: I (ads)-catalyzed dissolution and reordering of ion-bombarded Pd (111)," *Journal of Electroanalytical Chemistry,* vol. 381, pp. 239-241, 1995/01/24 1995.

[7] M. Grdeń*, et al.*, "Electrochemical behaviour of palladium electrode: Oxidation, electrodissolution and ionic adsorption," *Electrochimica Acta,* vol. 53, pp. 7583-7598, 11/1/ 2008.

[8] C. L. Scortichnini and C. N. Reilley, "Surface characterization of Pt electrodes using underpotential deposition of H and Cu," *Journal of Electroanalytical Chemistry and Interfacial Electrochemistry,* vol. 139, pp. 233-245, 1982/10/25 1982.

[9] A. Vaskevich*, et al.*, "Underpotential-overpotential transition of silver overlayer on platinum Part 1. Formation of a Pt + Ag surface alloy," *Journal of Electroanalytical Chemistry,* vol. 383, pp. 167-174, 1995/02/21 1995.

[10] P. O. Andricacos and P. N. Ross, "The underpotential deposition of Cu on Pt single crystals prepared in an ultra-high vacuum system," *Journal of Electroanalytical Chemistry and Interfacial Electrochemistry,* vol. 167, pp. 301-308, 1984/06/08 1984.

[11] B. H. Davis, "A comparison of surface areas derived from mercury penetration and nitrogen adsorption," *Applied Catalysis,* vol. 10, pp. 185-198, 1984.

[12] G. Fagerlund, "Determination of specific surface by the BET method," *Matériaux et Construction,* vol. 6, pp. 239-245, 1973// 1973.

[13] L. Hernán*, et al.*, "Limitations in the use of X-ray crystallite size in the determination of surface area in Co3O4," *Journal of Colloid and Interface Science,* vol. 115, pp. 274-276, 1987.

[14] J. R. Anderson, *Structure of metallic catalysts*. London: Academic Press, 1975.

[15] T. A. Dorling and R. L. Moss, "The structure and activity of supported metal catalysts: II. Crystallite size and CO chemisorption on platinum/silica catalysts," *Journal of Catalysis,* vol. 7, pp. 378-385, 1967.

[16] S. J. Gregg and K. S. W. Sing, *Adsorption, Surface Area and Porosity*, 2nd ed. London: Academic Press Inc., 1982.
[17] S. Kerzenmacher*, et al.*, "Energy harvesting by implantable abiotically catalyzed glucose fuel cells," *Journal of Power Sources,* vol. 182, pp. 1-17, 2008.
[18] M. M. Collinson, "Nanoporous Gold Electrodes and Their Applications in Analytical Chemistry," *ISRN Analytical Chemistry,* vol. 2013, p. 21, 2013.
[19] L.-l. Fang*, et al.*, "Determination of the Real Surface Area of Palladium Electrode," *Chinese Journal of Chemical Physics,* vol. 23, p. 543, 2010.
[20] J. M. D. Cónsul*, et al.*, "NO reduction with CO on alumina-modified silica-supported palladium and molybdenum-palladium catalysts," *Applied Catalysis A: General,* vol. 339, pp. 151-158, 2008.
[21] R. L. Sacci, "Electrooxidation of carbon monoxide and formic acid on polycrystalline palladium," Doctor of Philosophy, Department of Chemistry, University of Victoria, 2012.
[22] S.-I. Choi*, et al.*, "A Comprehensive Study of Formic Acid Oxidation on Palladium Nanocrystals with Different Types of Facets and Twin Defects," *ChemCatChem,* vol. 7, pp. 2077-2084, 2015.
[23] E. Antolini, "Palladium in fuel cell catalysis," *Energy & Environmental Science,* vol. 2, pp. 915-931, 2009.
[24] W. Sriwatanapongse*, et al.*, "Reductive Hydrodechlorination of Trichloroethylene by Palladium-on-Alumina Catalyst: 13C Solid-State NMR Study of Surface Reaction Precursors," *Langmuir,* vol. 22, pp. 4158-4164, 2006.
[25] D. Monzón-Hernández*, et al.*, "Fast response fiber optic hydrogen sensor based on palladium and gold nano-layers," *Sensors and Actuators B: Chemical,* vol. 136, pp. 562-566, 3/2/ 2009.
[26] S. Henning*, et al.*, "Bulk-Palladium and Palladium-on-Gold Electrocatalysts for the Oxidation of Hydrogen in Alkaline Electrolyte," *Journal of The Electrochemical Society,* vol. 162, pp. F178-F189, January 1, 2015 2015.
[27] I. T. McCrum and M. J. Janik, "First Principles Simulations of Cyclic Voltammograms on Stepped Pt (553) and Pt (533) Electrode Surfaces," *ChemElectroChem,* vol. 3, pp. 1609-1617, 2016.
[28] I. T. McCrum and M. J. Janik, "Deconvoluting Cyclic Voltammograms To Accurately Calculate Pt Electrochemically Active Surface Area," *The Journal of Physical Chemistry C,* vol. 121, pp. 6237-6245, 2017/03/23 2017.
[29] R. Woods, "Chemisorption at Electrodes: Hydrogen and Oxygen on Noble Metals and their Alloys," in *Electroanalytical chemistry: a series of advances*. vol. 9, A. J. Bard, Ed., ed New York: Dekker, 1976, pp. 1-162.
[30] B. Piela and P. K. Wrona, "Capacitance of the gold electrode in 0.5 M H2SO4 solution: a.c. impedance studies," *Journal of Electroanalytical Chemistry,* vol. 388, pp. 69-79, 5/16/ 1995.
[31] ZAHNER, "Thales manual," 2013.
[32] G. J. Brug*, et al.*, "The analysis of electrode impedances complicated by the presence of a constant phase element," *Journal of Electroanalytical Chemistry and Interfacial Electrochemistry,* vol. 176, pp. 275-295, 1984/09/25/ 1984.
[33] F. Seland*, et al.*, "Impedance study of methanol oxidation on platinum electrodes,"

Electrochimica Acta, vol. 51, pp. 3827-3840, 5/5/ 2006.
[34] B. Łosiewicz*, et al.*, "Effect of adsorbed carbon monoxide on the kinetics of hydrogen electrosorption into palladium," *Journal of Electroanalytical Chemistry,* vol. 611, pp. 26-34, 12/15/ 2007.
[35] A. Merkoci, *Biosensing using nanomaterials*. New Jersey: John Wiley & Sons, Inc, 2009.
[36] P. D. Pletcher*, et al.*, *Instrumental Methods in Electrochemistry*. Southampton Electrochemistry Group: Woodhead Publishing, Oxford, 2011.
[37] A. J. Bard and L. R. Faulkner, *Electrochemical Methods*, 2 ed. Hoboken: John Wiley & Sons Inc., 2001.
[38] S. J. Konopka and B. McDuffie, "Diffusion coefficients of ferri- and ferrocyanide ions in aqueous media, using twin-electrode thin-layer electrochemistry," *Analytical Chemistry,* vol. 42, pp. 1741-1746, 1970/12/01 1970.
[39] S. Wu*, et al.*, "Deposition and diffusion of plasma sputtered platinum nanoparticles in porous anodic alumina oxide.," *Journal of Optoelectronics and Advanced Materials,* vol. 12, pp. 451-455, 2010.
[40] J. Shen*, et al.*, "AFM tip-sample convolution effects for cylinder protrusions," *Applied Surface Science,* vol. 422, pp. 482-491, 2017/11/15/ 2017.
[41] J. Shen*, et al.*, "AFM characterization of patterned sapphire substrate with dense cone arrays: Image artefacts and tip-cone convolution effect," *Applied Surface Science,* vol. 433, pp. 358-366, 2018/03/01/ 2018.
[42] B. E. Conway, "Electrochemical oxide film formation at noble metals as a surface-chemical process," *Progress in Surface Science,* vol. 49, pp. 331-452, 1995/08/01/ 1995.
[43] A. Farkas*, et al.*, "On the Platinum-Oxide Formation under Gas-Phase and Electrochemical Conditions," *Journal of Electron Spectroscopy and Related Phenomena,* 2017/07/03/ 2017.
[44] A. J. Zhang*, et al.*, "Growth of thin, hydrous oxide films at Pd electrodes," *Journal of Electroanalytical Chemistry,* vol. 389, pp. 149-159, 1995/06/01/ 1995.
[45] D. A. J. Rand and R. Woods, "A study of the dissolution of platinum, palladium, rhodium and gold electrodes in 1 m sulphuric acid by cyclic voltammetry," *Journal of Electroanalytical Chemistry and Interfacial Electrochemistry,* vol. 35, pp. 209-218, 1972/03/01/ 1972.
[46] F. Gołek*, et al.*, "AFM image artefacts," *Applied Surface Science,* vol. 304, pp. 11-19, 2014/06/15/ 2014.
[47] A. Gruber*, et al.*, "Nanostructures produced by cluster beam lithography," *Applied Physics A,* vol. 68, pp. 197-201, 1999/02/01 1999.
[48] S. B. Velegol*, et al.*, "AFM Imaging Artefacts due to Bacterial Cell Height and AFM Tip Geometry," *Langmuir,* vol. 19, pp. 851-857, 2003/02/01 2003.
[49] Y. Wu*, et al.*, "The analysis of morphological distortion during AFM study of cells," *Scanning,* vol. 30, pp. 426-432, 2008.
[50] P. A. Maurice, "Applications of atomic-force microscopy in environmental colloid and surface chemistry," *Colloids and Surfaces A: Physicochemical and Engineering Aspects,* vol. 107, pp. 57-75, 1996/02/20/ 1996.
[51] W. Vastarella*, et al.*, "Integration Between Template-Based Nanostructured Surfaces and Biosensors," in *Biosensing Using Nanomaterials*, ed: John Wiley & Sons, Inc., 2009, pp.

377-419.
[52] K. Ngamchuea*, et al.*, "Planar diffusion to macro disc electrodes—what electrode size is required for the Cottrell and Randles-Sevcik equations to apply quantitatively?," *Journal of Solid State Electrochemistry,* vol. 18, pp. 3251-3257, 2014// 2014.
[53] A. Czerwiński, "The adsorption of carbon oxides on a palladium electrode from acidic solution," *Journal of Electroanalytical Chemistry,* vol. 379, pp. 487-493, 1994/12/12/ 1994.
[54] R. Buividas*, et al.*, "Novel method to determine the actual surface area of a laser-nanotextured sensor," *Applied Physics A,* vol. 114, pp. 169-175, 2013.

Figure legends

Figure 1: An electrical equivalent circuit of the Pd electrodes.

Figure 2: Surface topography of the electrodes with (a) 100 nm and (b) 200 nm pores covered with a 100 nm thick layer of Pd. The surface topography of the electrodes with (c) 100 nm and (d) 200 nm pores covered with 200 nm thick layer of Au. The *insets* show EDS analysis of the electrode surface.

Figure 3: AFM images obtained from the electrode surface. Column 1 shows the topography of the electrodes made from AAO substrates with 100 nm pores. Column 2 shows the topography of electrodes made from AAO substrates with 200 nm pores. Figure (a) and (b) shows the topography of native membranes, (c) and (d) shows the topography after deposition of 100 nm Pd, and (e) and (f) shows the topography after deposition of 200 nm Au.

Figure 4: The surface area ratio of the Au and Pd electrodes based on (a) 2D SEM image analysis, and (b) 3D AFM image analysis.

Figure 5: CV curves showing (1) oxide formation and (2) oxide reduction in 0.5 M H_2SO_4 of (a) Pd electrodes and (b) Au electrodes with 100 and 200 nm pores. The scan rate was 50 mVs^{-1}. The arrow shows the scan direction.

Figure 6: EIS curves of (a) the Pd with 100 and 200 nm pores with the curve fitting based on the equivalent circuit (figure 1), and (b) the Au electrodes with 100 and 200 nm pores based on the equivalent circuit shown in inset (ii). The full extension of the EIS curves from the Au electrodes are shown in inset (i).

Figure 7: CV curves in 1 M H_2SO_4 showing the oxidation of iodine-adsorbed to (a) Pd and (b) Au electrodes with 100 and 200 nm pores. The plots associated with untreated electrodes are superimposed. The scan rate is 10 mVs^{-1}**.** The arrow shows the scan direction.

Figure 8: Peak currents as function of the square root of the scan rate from (a) Pd coated electrodes and (b) Au coated electrodes. Top LHC insets show the original CVs obtained from electrodes with (i) 100 nm and (ii) 200 nm pores, with the scan direction shown by the arrow. The bottom RHC insets show (iii) the real surface areas obtained from the linear slopes using the Randles–Sevcik equation.

Figure 9: Comparative analysis of the different methods used to determine the real surface area in this study. The black bar on the centre top surface of the columns represents the standard error of the mean (n = 3).

Table 1: Summary of surface area ratios vs the area determination methods.

Figures

Figure 1

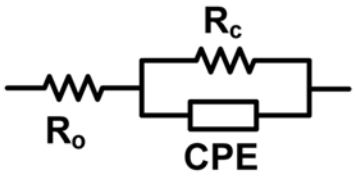

Figure 2

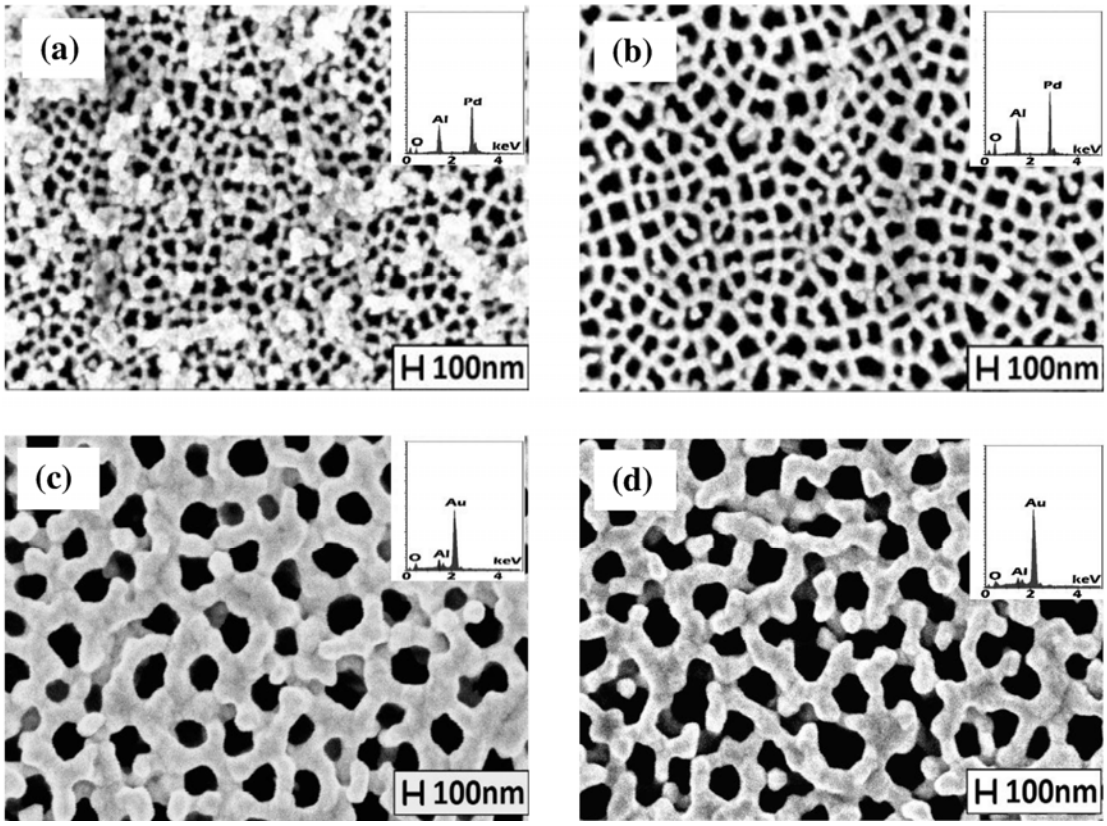
(a)
Pd
Al
O
keV
0
2
4
H 100nm
(b)
Pd
Al
O
keV
0
2
4
H 100nm
(c)
Au
O
Al
keV
0
2
4
H 100nm
(d)
Au
O
Al
keV
0
2
4
H 100nm

Figure 3

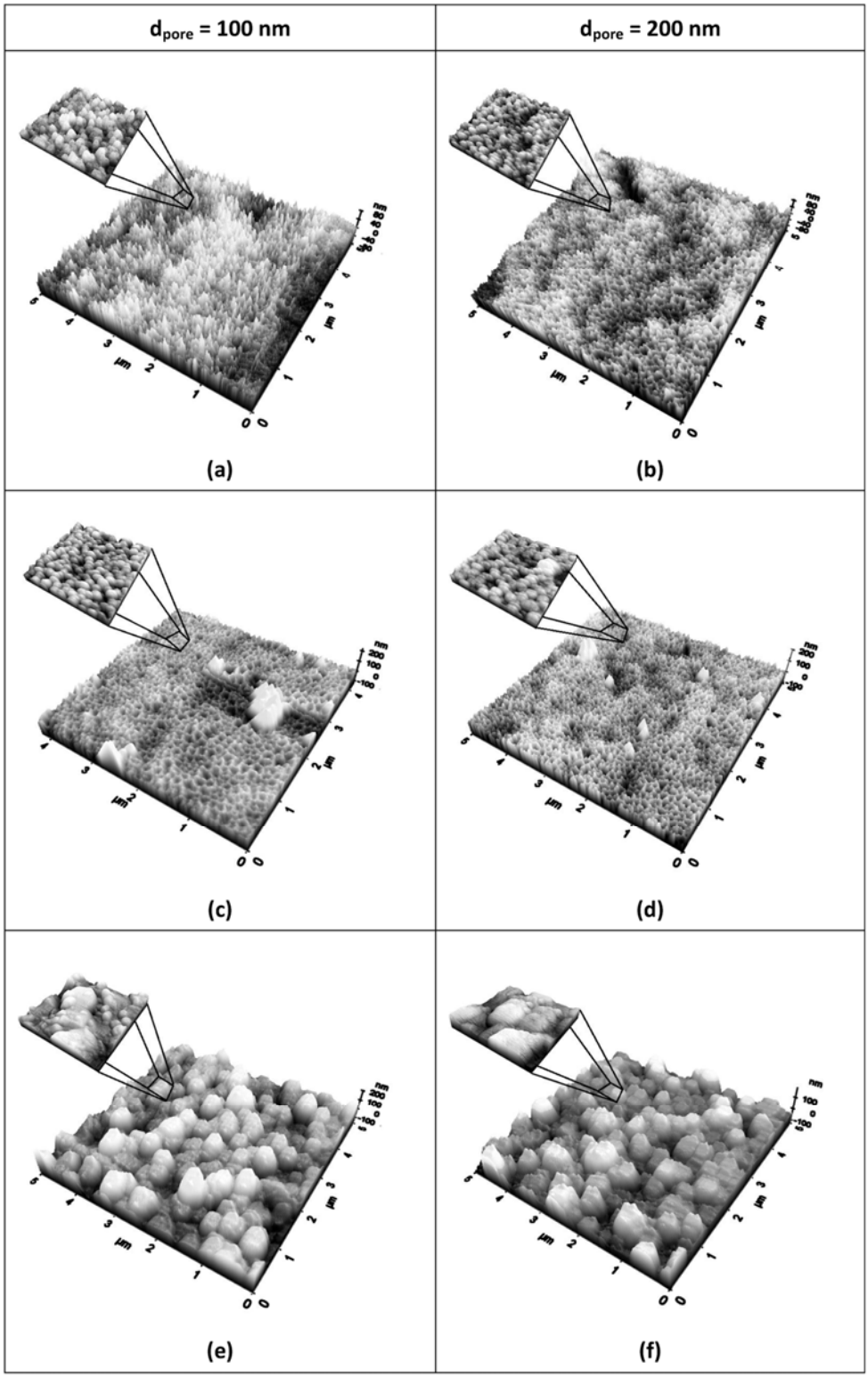

Figure 4

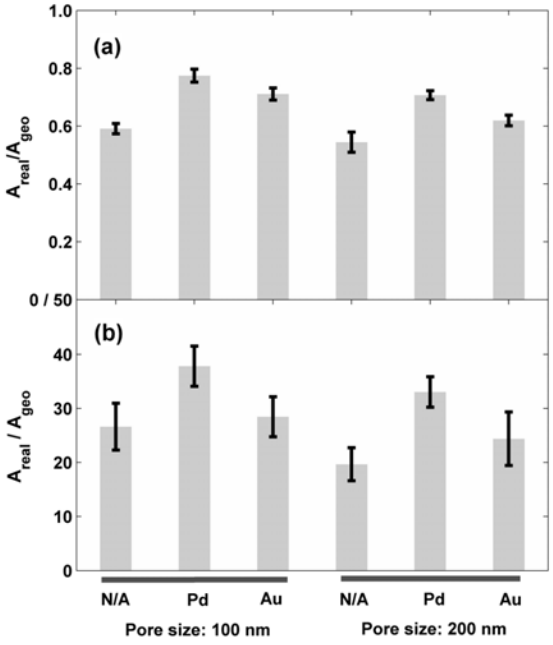
(a)
(b)
A_{real}/A_{geo}
A_{real}/A_{geo}
1.0
0.8
0.6
0.4
0.2
0 / 50
40
30
20
10
0
N/A
Pd
Au
N/A
Pd
Au
Pore size: 100 nm
Pore size: 200 nm

Figure 5

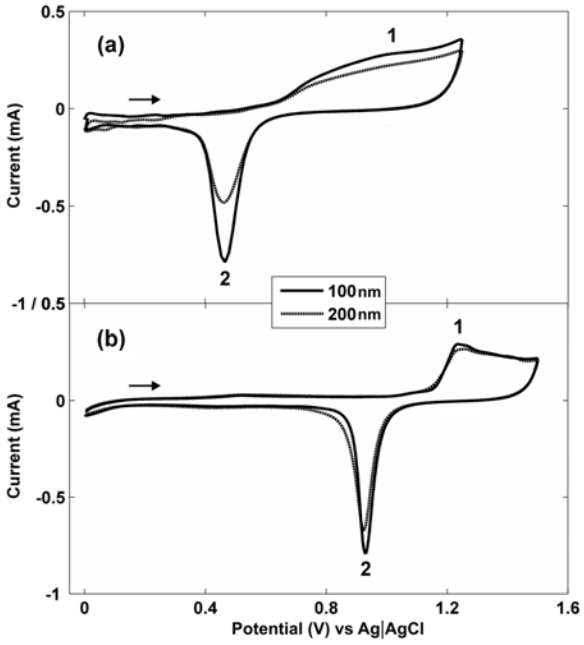
(a)
(b)
1
2
100nm
200nm
Current (mA)
Potential (V) vs Ag|AgCl
0.5
0
-0.5
-1 / 0.5
-1
0.4
0.8
1.2
1.6

Figure 6

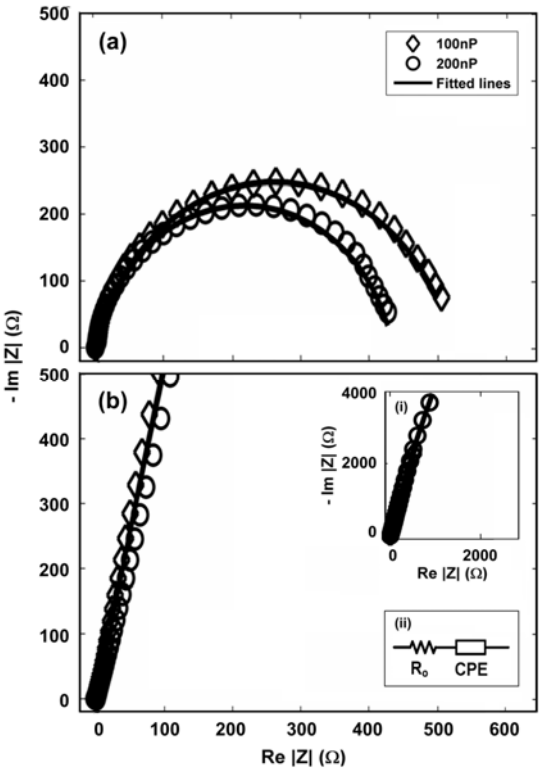

Figure 7

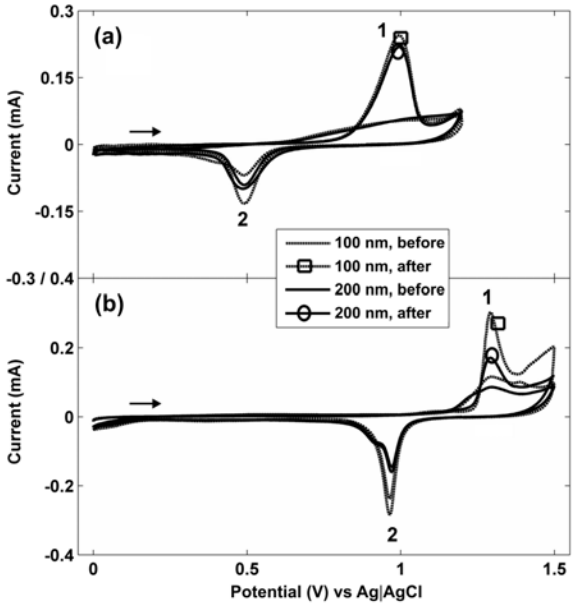
(a)
(b)
1
2
Current (mA)
Potential (V) vs Ag|AgCl
100 nm, before
100 nm, after
200 nm, before
200 nm, after
0.3
0.15
0
-0.15
-0.3 / 0.4
0.2
-0.2
-0.4
0.5
1
1.5

Figure 8

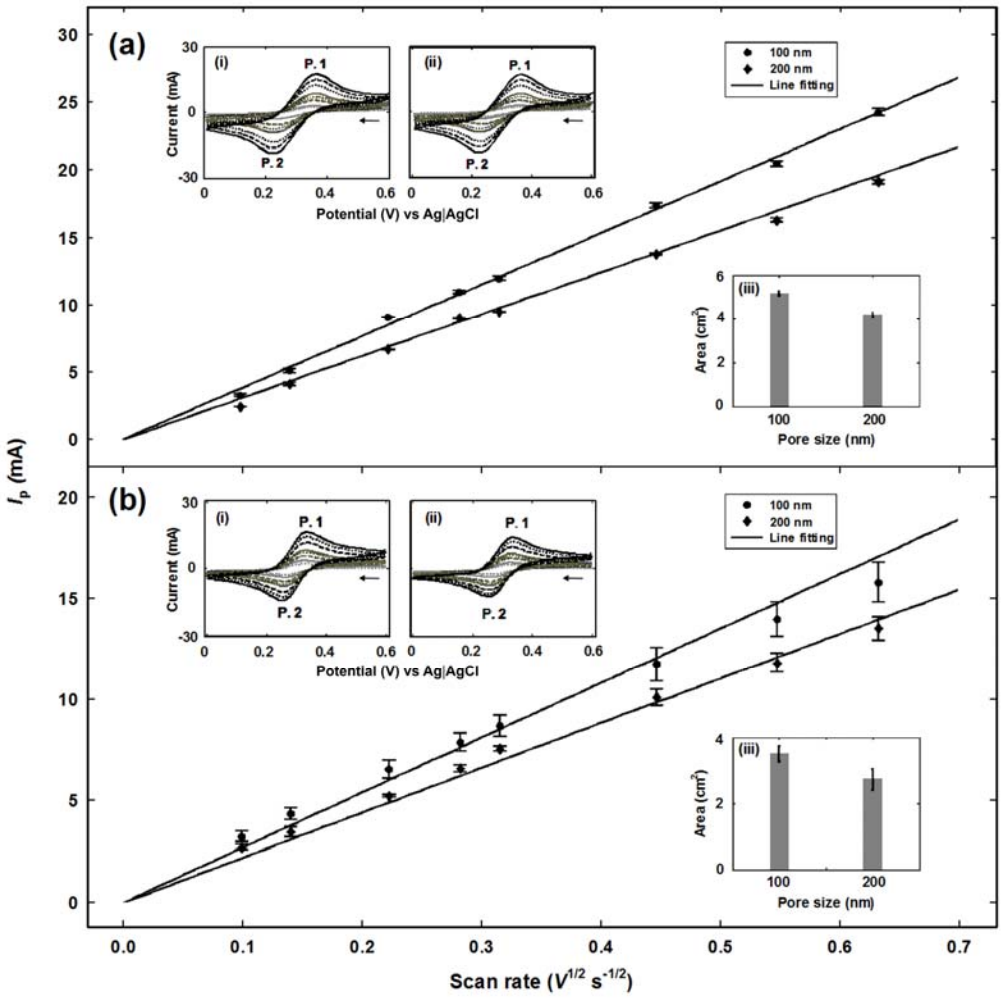
(a)
(b)
(i)
(ii)
(iii)
P. 1
P. 2
100 nm
200 nm
Line fitting
Current (mA)
Potential (V) vs Ag|AgCl
Area (cm²)
Pore size (nm)
I_p (mA)
Scan rate ($V^{1/2}$ $s^{-1/2}$)

Figure 9

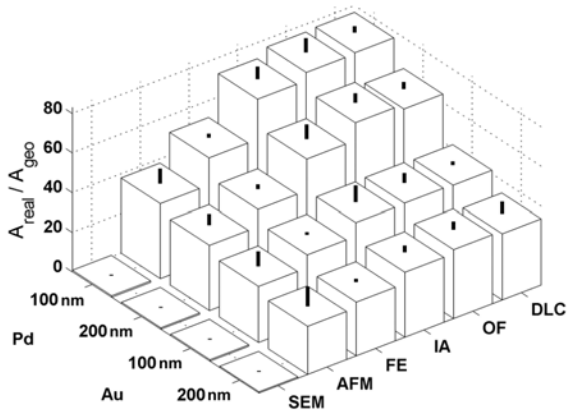
80
60
40
20
0
A_{real} / A_{geo}
100 nm
200 nm
Pd
100 nm
200 nm
Au
SEM
AFM
FE
IA
OF
DLC

Table 1

Table 1: Summary of surface area ratios vs the area determination methods.

Electrode Material	Pore size	Surface area determination method					
		SEM	AFM	FE	IA	OF	DLC
Pd	100 nm	0.8 ± 0.4	37.8 ± 7.4	51.4 ± 2.7	71.8 ± 6.3	75.4 ± 2.3	76.5 ± 3.1
	200 nm	0.7 ± 0.3	33.0 ± 5.6	41.7 ± 3.2	57.6 ± 7.2	66.3 ± 7.0	64.1 ± 3.4
Au	100 nm	0.7 ± 0.4	28.4 ± 7.4	34.9 ± 1.9	41.8 ± 8.3	42.0 ± 3.3	41.7 ± 1.7
	200 nm	0.6 ± 0.3	24.4 ± 9.9	27.8 ± 2.7	32.9 ± 3.3	34.7 ± 1.3	33.5 ± 5.9